THE JOURNAL OF PHYSICAL CHEMISTRY LETTERS
A JOURNAL OF THE AMERICAN CHEMICAL SOCIETY

pubs.acs.org/JPCL

Letter

Quantifying the Nearly Random Microheterogeneity of Aqueous *tert*-Butyl Alcohol Solutions Using Vibrational Spectroscopy

Andres S. Urbina, Lyudmila V. Slipchenko, and Dor Ben-Amotz*

Cite This: *J. Phys. Chem. Lett.* 2023, 14, 11376−11383

Read Online

ACCESS | Metrics & More | Article Recommendations | Supporting Information

ABSTRACT: The microheterogeneous structure of aqueous *tert*-butyl alcohol (TBA) solutions is quantified by combining experimental, simulations, and theoretical results. Experimental Raman multivariate curve resolution (Raman-MCR) C−H frequency shift measurements are compared with predictions obtained using combined quantum mechanical and effective fragment potential (QM/EFP) calculations, as well as with molecular dynamics (MD), random mixture (RM), and finite lattice (FL) predictions. The results indicate that the microheterogeneous aggregation in aqueous TBA solutions is slightly less than that predicted by MD simulations performed using either CHARMM generalized force field (CGenFF) or optimized parameters for liquid simulations all atom (OPLS-AA) force fields but slightly more than that in a self-avoiding RM of TBA-like molecules. The results imply that the onset of microheterogeneity in aqueous solutions occurs when solute contact free energies are about an order of magnitude smaller than thermal fluctuations, thus suggesting a fundamental bound of relevance to biological self-assembly.

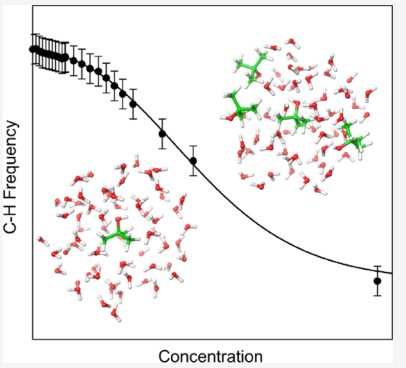

Water-mediated self-assembly is a ubiquitous feature of biological and other processes including micelle formation and liquid−liquid phase separation.[1,2] However, the contact free energy threshold associated with the emergence of such nonrandom microheterogeneous structures in fluid mixtures remains an open question. Here we address this question using infinitely miscible aqueous *tert*-butyl alcohol (TBA) solutions, for which prior experimental and simulation studies have found evidence of slight (nearly random) microheterogeneity[3−6] that is on the verge of undergoing liquid-phase separation.[2,7−11] To more definitively characterize the microheterogeneity of aqueous TBA solutions, we quantify TBA−TBA contact statistics and free energies using Raman multivariate curve resolution (Raman-MCR) C−H frequency shift measurements, combined with molecular dynamics (MD), random mixture (RM), and finite lattice (FL)[12−14] simulations, as well as hybrid quantum mechanical and effective fragment potential (QM/EFP) based normal mode and local mode vibrational frequency calculations. Comparisons of the predicted and measured C−H frequency shifts with FL predictions are used to quantify TBA contact distributions and establish a contact free energy bound on water-mediated self-assembly.

Prior vibrational and NMR spectroscopic,[4,6,10,11] neutron,[15,16] X-ray,[10] light scattering,[16−18] and simulation[2,7−9,20] studies of aqueous TBA have found evidence of TBA aggregation that has variously been described as containing long-range correlations (>10 nm),[2] micelle-like structures,[16] or a nearly RM structure.[2,4] The present experimental, simulation, and theoretical analysis aims to quantitatively compare the microheterogeneity in aqueous TBA with that predicted by using RM and MD models. The MD simulations are performed using the same CHARMM generalized force field (CGenFF) that was found to produce large-scale simulation predictions that are consistent with experimental miscibility, neutron and X-ray scattering measurements,[2] as well as an optimized parameters for liquid simulations all atom (OPLS-AA) force field[8] that produces quite similar predictions. Figure 1 shows representative MD snapshots corresponding to TBA molecules with two different numbers of nearest neighbor contacts, (a) $k = 0$ and (b) $k = 3$. The present FL model of TBA aggregation[12−14] is found to accurately replicate both the simulation and experimental results, thus providing a quantitative measure of the TBA nearest neighbor contact probability distributions, $P(k)$, as well as the associated contact free energy and the onset of microheterogeneity.

In the FL model,[12−14] the first coordination shell of TBA is represented as an icosahedral lattice with 12 lattice sites and 5 nearest neighbors per lattice site.[12] The FL aggregation statistics are influenced by the contact energy ε_1 between the central TBA and each of its TBA-occupied coordination-shell lattice sites, as well as the contact energy ε_2 between

Received: November 2, 2023
Revised: December 6, 2023
Accepted: December 7, 2023
Published: December 11, 2023

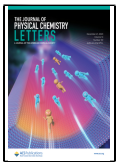

https://doi.org/10.1021/acs.jpclett.3c02603
J. Phys. Chem. Lett. 2023, 14, 11376−11383

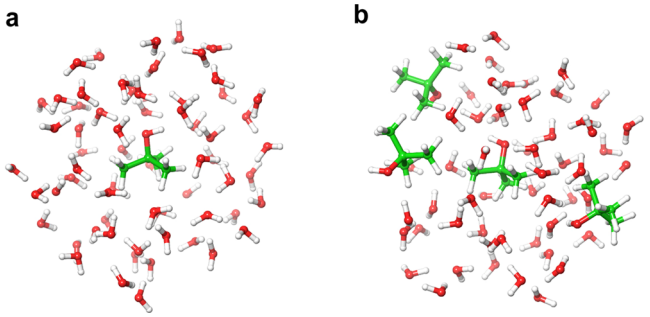

Figure 1. Simulation snapshots from aqueous TBA solutions in which the central TBA has either (a) $k = 0$ or (b) $k = 3$ nearest neighbor contacts (within 0.75 nm of the central TBA).

neighboring occupied sites within the coordination shell of the central TBA. Unless noted otherwise, we will assume that the two energies are the same, $\varepsilon = \varepsilon_1 = \varepsilon_2$ since they both pertain to TBA−TBA contacts. However, in general, ε_1 and ε_2 need not be the same if cooperative (or anticooperative) effects produce a significant change in binary contact free energy with increasing concentration. Although ε represents the contact energy between sites in an idealized lattice composed of featureless particles, when applied to molecular aggregation processes, ε represents a free energy that may be influenced by both the energy and entropy associated with the formation of a contact between neighboring TBA molecules. Moreover, the FL model explicitly includes the influence of the additional configuration entropy associated with the statistical distribution of the aggregate structures, as further described in Methods (and previous publications).[12−14]

Figure 2 shows the TBA−TBA central−carbon radial distribution functions, $g(r)_{C-C}$, and the resulting contact probability distributions, $P(k)$, obtained from either MD or RM simulations and FL predictions. Note that MD $g(r)_{C-C}$, shown in Figure 2a, contains a sharp first peak near $r = 0.5$ nm arising from TBA molecules that are directly hydrogen-bonded to each other. The marked concentration dependence of the third peak in $g(r)_{C-C}$ (between $r = 0.8$ and 1 nm) is linked to the onset of significant TBA aggregation above 1 M (as the peak near $r = 0.9$ nm pertains to water-separated TBA molecules, while that near 1 nm pertains to TBA-separated TBA molecules). The vertical dotted lines in Figure 2a,b mark the boundaries of the first coordination shell (at $r = 0.468$ and 0.75 nm) used to establish the FL cell volume and athermal ($\varepsilon = 0$) filling fraction, obtained as further described in Methods. The $P(k)$ distribution points shown in the lower two panels of Figure 2 were obtained by counting all TBA molecules whose central carbons are within 0.75 nm of a given TBA molecule. The solid curves of Figure 2c,d are FL model predictions obtained from fits to experimental C−H frequency shifts, and the dashed curves in panel d are athermal FL predictions (obtained as further described below and in Methods).

Figure 3 compares predicted and measured C−H vibrational spectra and mean frequencies. The upper two panels show QM/EFP Raman normal mode spectral predictions, with prominent symmetric (lower frequency) and asymmetric (higher frequency) sub-bands, obtained from configurations

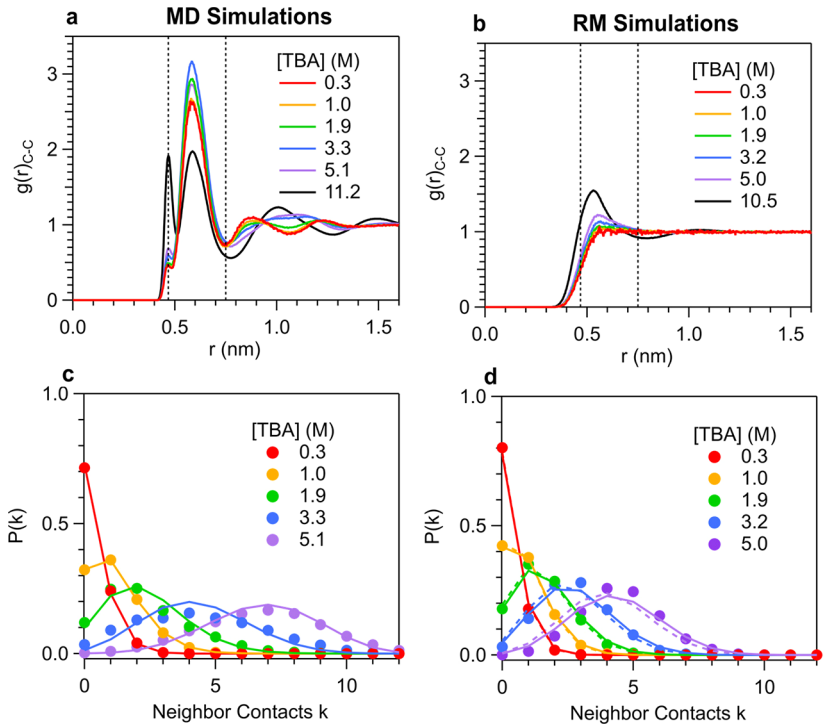

Figure 2. Comparison of MD, RM, and FL predictions. The upper two panels show the central carbon radial distribution functions from (a) aqueous TBA MD simulations and (b) a self-avoiding RM of TBA-like molecules, as a function of TBA concentration, up to pure liquid TBA. The vertical dashed lines represent the inner and outer boundaries of the first coordination shell of TBA at 0.468 and 0.75 nm. The lower two panels show the nearest neighbor contact distributions in (c) MD and (d) RM simulations, where k is the number of TBA molecules that are within 0.75 nm of a given TBA. The solid curves in the lower two panels are FL predictions with TBA contact free energies of (c) $\beta\varepsilon = -0.25$ and (d) $\beta\varepsilon = -0.04$ whose values are obtained from FL fits to the corresponding TBA C−H vibrational frequency shift predictions (and the dashed curves are athermal, $\beta\varepsilon = 0$, FL predictions), as further described below and in Methods.

https://doi.org/10.1021/acs.jpclett.3c02603
J. Phys. Chem. Lett. 2023, 14, 11376−11383

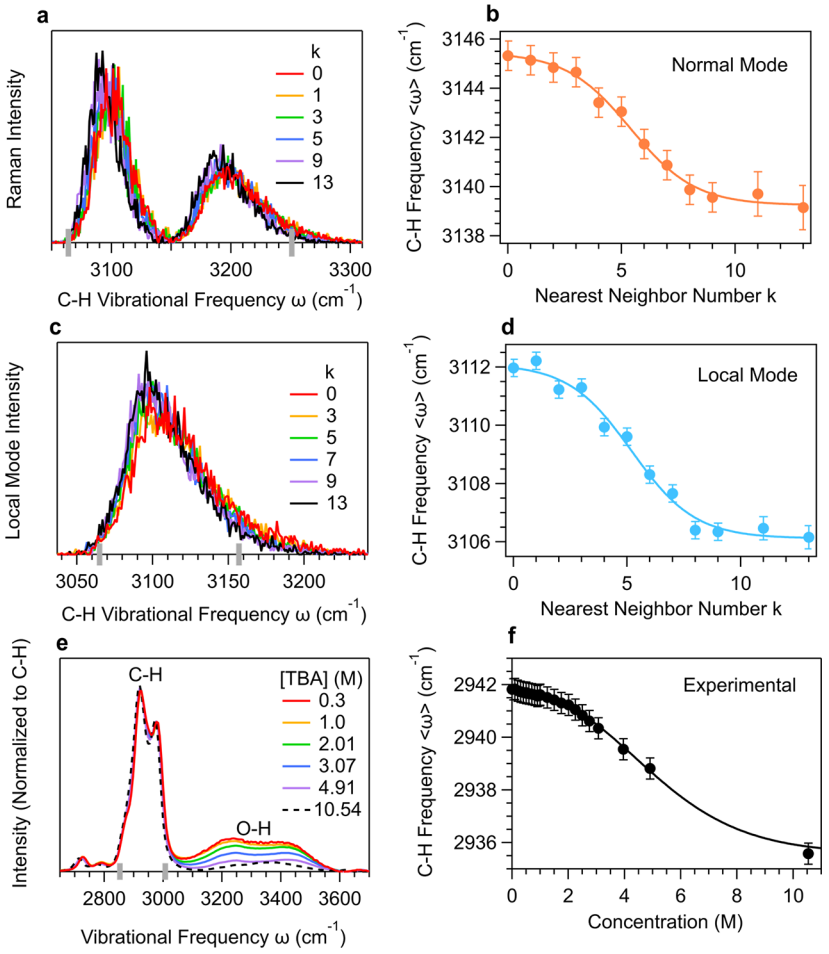

Figure 3. Comparison of the calculated and measured TBA C−H vibrational spectra and frequency shifts. The upper two panels show QM/EFP calculated (a) Raman normal mode (full Hessian) spectra and (b) the resulting C−H mean frequency shift as a function of k. The middle two panels show the QM/EFP calculated (c) local mode (partial Hessian) spectra and (d) the resulting C−H mean frequency shift as a function of k. The lower two panels show experimentally measured (e) Raman-MCR spectra in the C−H and the O−H stretch band region and (f) the resulting C−H mean frequency shift as a function of TBA concentration. The gray bars on the frequency axis in panels a, c, and e mark the frequency ranges over which the mean C−H frequencies were calculated, as further described in Methods.

with different numbers of TBA nearest neighbor contacts k. The middle two panels show the corresponding C−H local mode predictions. The lower two panels show experimental C−H (and O−H) bands in the Raman-MCR SC spectra of aqueous TBA (obtained as described in Methods and ref 4). Although the mean C−H frequencies $\langle\omega\rangle$ shown in the right-hand panels of Figure 3 are not the same for the normal mode, local mode, and experimental measurements, the corresponding frequency shifts, relative to a dilute aqueous TBA solution, are very similar, as further explained below and shown in Figure 4a.

Figure 4 compares predicted and experimental results for the TBA C−H frequency shift, $\Delta\omega$, and average number of nearest neighbor contacts, $\langle k\rangle$, in aqueous TBA solutions with concentrations up to 5 M. The upper two panels in Figure 4 show $\Delta\omega$ plotted as a function of (a) the number of neighbor contacts k or (b) TBA concentration. The points in Figure 4a show the excellent agreement between the normal and local mode frequency shifts, and the dotted curves are fits to a zero-intercept Sigmoidal function of the form

$$\Delta\omega(k) = a_1\left[\frac{1}{1 + e^{-(k-a_2)/a_3}} - \frac{1}{1 + e^{a_2/a_3}}\right]$$

(with parameters given in the caption of Figure 4). Essentially perfect agreement between the normal mode and local mode shifts can be obtained by slightly varying the frequency range over which $\langle\omega\rangle$ is evaluated, and somewhat larger shift predictions are obtained when extending the frequency range to higher frequencies (that were excluded from the $\langle\omega\rangle$ calculations because that region of the experimental C−H band is not accessible due to overlap with the O−H band). The solid curves in Figure 4b are FL predictions obtained (as described in Methods) assuming contact free energies $\varepsilon/RT = \beta\varepsilon_1 = \beta\varepsilon_2$ chosen to approximately reproduce the MD (orange), RM (light blue), and experimental (black) $\Delta\omega_k$ results, and the dashed green curves in Figure 4b,d pertain to athermal FL predictions (with $\varepsilon/RT = 0$).

The MD and RM frequency shift predictions shown in Figure 4b were obtained using eqs 1 and 2 (in Methods), by combining $P(k)$ simulation results shown in Figure 2c,d, with the k-dependent C−H frequency shift predictions shown in Figure 4a. Panels c and d of Figure 4 show the experimentally derived $P(k)$ and $\langle k\rangle$ predictions, respectively, obtained by using the FL fits to the frequency shift results in Figure 4b. The $P(k)$ predictions in Figure 4c imply that aqueous TBA aggregates have a percolation threshold near 2 M, correspond-

https://doi.org/10.1021/acs.jpclett.3c02603
J. Phys. Chem. Lett. 2023, 14, 11376−11383

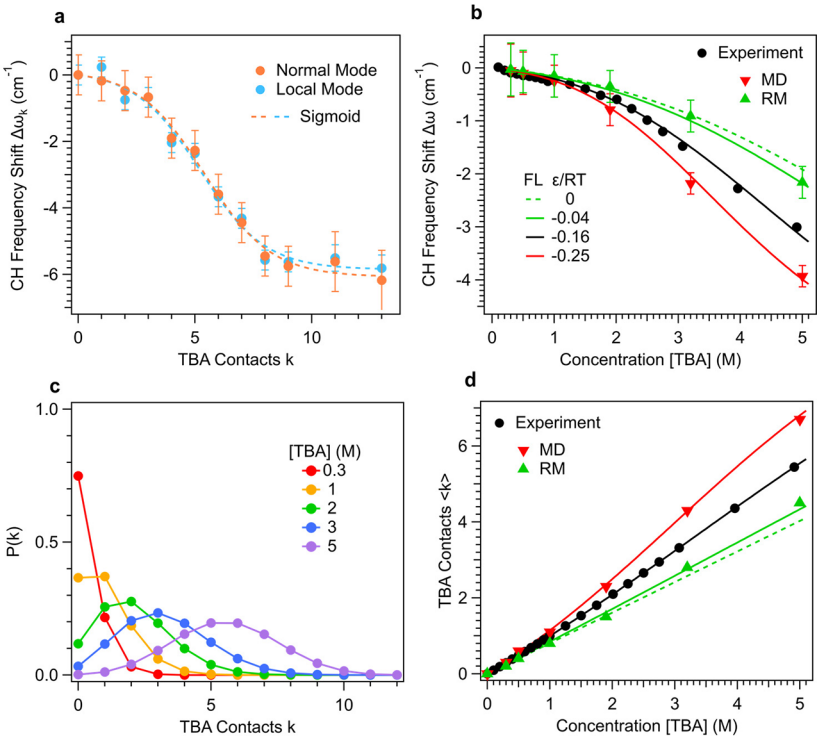

Figure 4. Normal and local mode frequency shift predictions are used to obtain experimental, MD, RM, and FL contact free energies and nearest neighbor distributions. (a) Comparison of normal and local mode C−H vibrational frequency shift points and Sigmoidal fit dashed curves (with normal mode fit parameters $a_1 = -6.21$, $a_2 = 5.408$, and $a_3 = 1.419$). (b) Calculated and experimental vibrational C−H frequency shifts plotted as a function of TBA concentration. The curves are FL predictions obtained using the ϵ/RT values indicated in the figure legend. (c) Experimentally derived $P(k)$ distributions obtained from FL fits to the experimental $\Delta\omega$ shown in panel b. (d) Average number of TBA molecules in the first coordination shell of a given TBA, $\langle k \rangle$, as a function of the TBA concentration. The MD (red) and RM (green) $\langle k \rangle$ points are obtained from the corresponding $P(k)$ distributions, shown in Figure 2c,d. All of the curves in panel d (as well as the black points) are FL predictions obtained using the ϵ/RT values in the legend of panel b.

ing to the concentration at which $P(k)$ has a maximum at $k = 2$, as further shown and explained in SI Figure S3.

The nearly random microstructure of aqueous TBA implies that the onset of microheterogeneity—a precursor to self-assembly—occurs in aqueous solutions with negative solute contact free energies near $\beta\epsilon \sim -0.1$, or $\epsilon \sim -RT/10$. Our MD results imply that slightly larger contact free energies of $\epsilon \sim -RT/4$ ($\beta\epsilon \sim -0.25$) lead to greater microheterogeneity, while prior simulations of aqueous TBA solutions with slightly different force fields have been found to phase separate at room temperature.[2,7,8] A similar conclusion pertains to micelle formation, whose surfactant chemical potentials are of the order of $-RT$ lower in the micelle than for a free surfactant,[1] implying negative surfactant−surfactant contact free energies whose magnitudes are smaller than (or of the order of) RT. This suggests that the subtle microheterogeneity in aqueous TBA may be quite rare, as solutions with weaker solute-contact free energies will form essentially random mixtures while those with slightly larger (more negative) contact free energies will either phase separate or self-assemble into more significantly heterogeneous structures such as micelles and higher-order multiscale assemblies.

The present results, as well as those of some previous studies,[4,5,7] imply that aqueous TBA solutions are slightly less heterogeneous than MD predictions obtained using a wide range of force fields,[2,7,8] most of which lead to phase separation rather than a single-phase solution at room temperature. These include MD simulations performed using the transferable potential for phase equilibria-united atom (TraPPE-UA) force field,[7,20] which should accurately represent the direct interactions between TBA molecules. Thus, the overstructuring or phase separation of the resulting MD predictions[7] suggests that water-mediated interactions[3] damp direct TBA−TBA interactions more strongly than predicted using any of the tested MD force fields. Although the reason for this increased damping has not been established, it implies that solute−water or water−water attractive interactions are increased in the hydration shell of oily solutes, perhaps resulting from a local increase in molecular polarizability or charge transfer.[21,22]

The present MD and experimental aqueous TBA results have been found to be consistent with FL predictions obtained assuming that $\varepsilon_1 = \varepsilon_2$. However, in general the latter two contact free energies need not be the same if the aggregation process is cooperative (or anticooperative) in the sense that the effective contact energy between TBA molecules depends on the degree of aggregation of the coordination shell surrounding the central TBA. This leads to aggregation behavior that is analogous to allosteric interactions between ligands bound to a protein, which may be either cooperative (if ε_2 is more negative than ε_1, implying that the first bound ligand increases the binding affinity of a second ligand) or anticooperative (if ε_2 is more negative than ε_1, implying the first bound ligand decreases the binding affinity of the second ligand). The present RM simulation results reveal evidence of cooperative aggregation, consistent with a more negative value of ε_2 than ε_1. Specifically, FL predictions similar to the green RM curves shown in Figure 4b,d are obtained with $\beta\varepsilon_1 = 0$ and

https://doi.org/10.1021/acs.jpclett.3c02603
J. Phys. Chem. Lett. 2023, 14, 11376−11383

$\beta\varepsilon_2 = -0.06$, consistent with the expectation that a self-avoiding RM should have a zero contact free energy at low concentration that becomes increasingly negative at higher concentrations due to entropic packing interactions. At still higher concentrations, near the ~10.5 M concentration of pure liquid TBA, the RM $P(k)$ and $\langle k \rangle$ simulation results are better reproduced by FL predictions with $\beta\varepsilon_1 = 0$ and $\beta\varepsilon_2 = -0.18$, consistent with an increase in entropic packing cooperativity with increasing concentration, as shown in SI Figure S2b.

In aqueous TBA solutions such cooperativity is apparently smaller, as predictions obtained with $\varepsilon_1 = \varepsilon_2$ are reasonably consistent with the MD and experimental results over the entire concentration range up to pure liquid TBA, as shown in SI Figures S1a and S2a. This apparently smaller cooperativity suggests that both water-mediated and TBA-mediated interactions damp the intrinsic attraction between isolated TBA molecules to a similar degree. Such damping,[3] which is analogous to the much larger water-mediated shielding of electrostatic interactions between ions, is a critical prerequisite for the formation of biological systems that necessarily rely on contact free energies smaller in magnitude than RT to facilitate the collective assembly of dynamically stable living structures.

METHODS

Experimental Measurements. Raman multivariate curve resolution (Raman-MCR) spectra of aqueous *tert*-butyl alcohol (TBA) solutions were obtained as previously described,[4,6,23] at a temperature of 20 °C, over a concentration range of 0.2 M to pure liquid TBA. Briefly, solutions were produced using *tert*-butyl alcohol BA (≥99.5% TBA, Sigma-Aldrich) and ultrapure water (Milli-Q UF Plus, 18.2 mΩ·cm resistance, Millipore). Each spectrum was measured using custom-built Raman spectrometer,[23] with a 514.5 nm Ar-ion excitation laser of 10−20 mW power at the sample and signal averaged for 5 min. Self-Modeling Curve Resolution (SMCR)[6,23,24] was used to decompose solution spectra into pure water and the solute-correlated (SC) components used to obtain TBA C−H average frequencies and frequency shifts.

Molecular Dynamics (MD) and Random Mixture (RM) Simulations. MD simulations were performed using GROMACS (version 2019.2) with force fields of either CGenFF or OPLS-AA for TBA and TIP4P-2005 for water.[25−29] Each MD simulation contained 200 TBA molecules and 40000, 20000, 10000, 5000, 2500, 1250, 625, and 300 water molecules, corresponding to TBA concentrations of approximately 0.3, 0.5, 1.0, 1.9, 3.3, 5.1, 6.9, and 8.7 M, respectively, when using the CGenFF force field (while when using the OPLS-AA force field, the last four concentrations are approximately 3.2, 5.0, 7.0, and 8.6 M, respectively). The MD simulations of pure TBA were performed using 500 molecules, corresponding to a concentration of 11.2 M when using the CGenFF, or 11.0 M when using the OPLS-AA. The CGenFF MD results Figures 2−4 are compared with those obtained using OPLS-AA in the SI (Figures S4 and S5).

After energy minimization, *NVT* equilibration was performed for 200 ps with a 1 fs time step. *NPT* production runs were performed for 500 ns, with a 2 fs time step (1 fs for pure TBA), a velocity rescale thermostat for temperature control (293.15 K) and Parrinello−Rahman barostat for pressure control (1 bar).[30,31] Bonds were constrained with the LINCS algorithm.[32] A 1 nm cutoff was used for the Lennard-Jones potentials. Electrostatic long-range interactions were treated with particle mesh Ewald (PME) summations with a real space cutoff of 1 nm.[33,34] In the second half of each production trajectory, the reference frame was shifted such that a TBA molecule is in the center of the box prior to performing the contact statistics and vibrational frequency analysis. Random mixing (RM) configurations corresponding to the concentrations of the MD simulations described above were generated by randomly inserting 200 TBA molecules into the corresponding boxes using the GROMACS *gmx insert-molecules* function. For each concentration, a total of 15000 snapshots were generated and combined into a trajectory file.

***P*(*k*) Distributions.** First coordination-shell contacts between TBA molecules are defined as occurring when the distance between the central-carbon atoms on neighboring TBA molecules is less than 0.75 nm, approximately equal to the first coordination shell minimum in the TBA−TBA central-carbon radial distribution function, as shown in Figure 2a. The nearest neighbor contact probability distributions $P(k)$ were determined by tabulating the number, k, of nearest neighbor TBA molecules around each TBA, and averaging 14500 snapshots at each TBA concentration. This procedure was performed by using the GROMACS *gmx select* function for both the MD and RM simulations.

QM/EFP Vibrational Frequency Calculations. 1000 MD snapshots with the same k (as shown in the SI Table S2) were reduced in size to include a central TBA molecule and all neighboring molecules whose atoms are within 0.75 nm of the central carbon on the central TBA (using the GROMACS *gmx select* function). For each snapshot, geometry optimization was performed on the central TBA molecule, followed by a full Hessian analysis, carried out using a hybrid QM/EFP method[35−38] as implemented on home-built version of the GAMESS suite of programs based on the 2018 R1 release.[39,40] More specifically, the geometry of the central TBA (the QM region) is described using second order Møller−Plesset perturbation theory (MP2) using the 6-311++G** basis set.[41] All of the water and TBA molecules in the coordination shell of the central TBA were modeled by EFP potentials.[42,43] Specifically, TBA and water geometries for EFP parameter computations were optimized with the MP2/cc-pVTZ level of theory. The EFP parameters were computed with the hybrid 6-31+G(d)/6-311++G(3df,2p) basis sets. QM-EFP coupling terms include electrostatic, polarization, and fitted exchange-repulsion terms, as implemented in ref.[44] Gaussian-type polarization damping was used to avoid overpolarization of the system.[45]

Representative examples of the resulting normal mode spectra are listed in Figure 3a. Additionally, local mode C−H frequency predictions were obtained using a partial Hessian vibrational analysis,[19,46] after geometry optimization (as described above). The local mode frequency of a given TBA methyl C−H bond was obtained while holding all other atoms fixed (in both the central TBA and surrounding TBA and water molecules).[47] The resulting local mode frequencies for all 9 of the methyl hydrogens of the central TBA are then averaged over 1000 configurations with the same k, to obtain spectra such as those shown in Figure 3c.

The local mode frequency calculations were found to be about 2 times more numerically efficient than the normal mode spectral calculations (including both Hessian and Raman calculations), in spite of the fact that each Raman normal mode spectral calculation is compared with the average of 9 independent C−H local mode spectral calculations for the

https://doi.org/10.1021/acs.jpclett.3c02603
J. Phys. Chem. Lett. 2023, 14, 11376−11383

TBA molecule with a given coordination-shell configuration. Although the calculated average normal and local mode frequencies were not the same, the resulting frequency shifts relative to dilute (fully hydrated) aqueous TBA were virtually identical. An additional potential advantage of local mode calculations is that they might be used to obtain localized molecular information regarding how the frequency of given bond, and the force along that bond,[48] depends on its location within solute and surrounding molecules. However, the numerical uncertainty of these calculations was too large to reliably obtain such information.

C−H Mean Frequencies and Shifts. The predicted mean C−H frequency $\langle\omega\rangle_k$ of a TBA molecule whose first coordination shell contains k other TBA molecules is calculated as follows

$$\langle\omega\rangle_k = \frac{\int_{\omega_1}^{\omega_2} \omega I(\omega, k)\, d\omega}{\int_{\omega_1}^{\omega_2} I(\omega, k)\, d\omega} \quad (1)$$

where the frequency bounds, ω_1 to ω_2, span the region over which the C−H band intensity differs significantly from the surrounding baseline (as indicated by the gray bars on the frequency axes in left-hand panels of Figure 3). A similar expression is used to obtain the experimental mean C−H frequency at a given TBA concentration, $\langle\omega\rangle_{[c]}$, by replacing $I(\omega,k)$ by the measured C−H band shape at a given TBA concentration, $I(\omega,[c])$, as shown in Figure 2c,d.

The predicted C−H frequency shift at a given concentration is obtained, as follows, by combining the calculated average frequency as a function of k with MD or RM simulation predictions of the nearest neighbor contacts probability distribution, $P(k)$, at the concentration of interest

$$\Delta\omega = \sum_{k=0}^{k_{max}} P(k)\, \Delta\omega_k \quad (2)$$

where $k_{max} \leq 16$ is the maximum number of TBA molecules that are observed to occupy the coordination shell of a given TBA molecule at the concentration of interest, $\Delta\omega_k = \langle\omega\rangle_k - \langle\omega\rangle_0$ and $\langle\omega\rangle_0$ is the frequency of a fully hydrated (infinitely dilute) aqueous TBA. Equation 2 $\Delta\omega$ predictions were obtained using $P(k)$ from MD, RM, or FL predictions, and $\Delta\omega_k$ was obtained from a Sigmoidal fit to the MD/QM/EFP predicted values of $\Delta\omega_k = \langle\omega\rangle_k - \langle\omega\rangle_0$, as further shown in Figure 4a and in its discussion. The experimental C−H frequency shift at a given TBA concentration is $\Delta\omega = \langle\omega\rangle_{[c]} - \langle\omega\rangle_0$, where $\langle\omega\rangle_0$ is the experimental average C−H frequency extrapolated to zero TBA concentration. Note that the right-hand side of eq 2 is equivalent to $\langle\omega\rangle_{[c]} - \langle\omega\rangle_0$. The use of eq 2 to obtain RM frequency shift predictions relies on the assumption that $\Delta\omega_k$ predictions obtained from MD Raman normal mode calculations may be used to predict frequency shifts pertaining to RM configurations with the same k value. Thus, although RM simulations do not include any water molecules, the corresponding RM frequency shifts pertain to hydrated RM configurations.

Finite-Lattice (FL) Predictions. Equation 3 is the FL expression for the probability distribution $P(k)$ that there will be k TBA molecules in the coordination shell around a given TBA in a system with an average coordination-shell site occupancy probability of $p = [c]V_1$ pertaining to an athermal lattice (with $\varepsilon = 0$), where $[c]$ is the bulk concentration of TBA and V_1 is the volume of each lattice site, and $\beta\varepsilon_i = \varepsilon_i/RT$. The coefficients n_J^k represent the number of configurations with a given value of J and k, where J is the number of contacts among TBA molecules in a coordination-shell around a given TBA, as previously tabulated for various FL geometries including n = 12 and c = 5 (icosahedral) and c = 3 (truncated tetrahedral) structures.[12]

$$P(k) = \frac{\left\{\left[\left(\frac{p}{1-p}\right)e^{-\beta\varepsilon_1}\right]^k\left[\sum_{J=0}^{J_{max}} n_J^k e^{-J\beta\varepsilon_2}\right]\right\}}{\sum_{k=0}^{n}\left\{\left[\left(\frac{p}{1-p}\right)e^{-\beta\varepsilon_1}\right]^k\left[\sum_{J=0}^{J_{max}} n_J^k e^{-J\beta\varepsilon_2}\right]\right\}} \quad (3)$$

When both contact energies are equal to zero ($\varepsilon_1 = \varepsilon_2 = 0$), the above expression reduces to the following contact probability distribution in an athermal FL:[12]

$$P(k) = \frac{n!p^k(1-p)^{n-k}}{k!(n-k)!} \quad (4)$$

The present FL predictions, obtained assuming an icosahedral lattice with n = 12 lattice sites and c = 5 nearest neighbors per lattice site,[12] are virtually indistinguishable from those obtained using an alternative truncated tetrahedral lattice structure with n = 12 and c = 3,[12] with the magnitude of ε_2 is increased by a factor of 5/3 (equal to the ratio of the c values for the two lattices). Note that only ε_2 is changed since c dictates the number of possible ε_2 contacts between coordination-shell molecules, while ε_1 pertains to the energy of each of the n possible contacts between a central TBA molecule and TBA molecules in its first coordination-shell (and the above two lattices have the same value of n = 12). Thus, decreasing the number of possible coordination-shell contacts has the same effect as increasing the magnitude of the free energy per coordination-shell contact, with otherwise nearly identical FL predictions.

The FL frequency shift predictions were obtained assuming a limiting frequency shift at $k = n$ = 12 that is close to 6 cm^{-1}, slightly adjusted to produce approximate agreement with the frequency shift in pure liquid TBA, as shown in the SI Figure S1a. Specifically, the limiting k = 12 frequency shifts for the FL fits to the MD, RM and experimental results are 6.0, 6.4, and 6.3 cm^{-1}, respectively, whose small differences did not significantly influence the FL predictions below 5 M.

■ ASSOCIATED CONTENT

Supporting Information

The Supporting Information is available free of charge at https://pubs.acs.org/doi/10.1021/acs.jpclett.3c02603.

Additional comparisons of calculated and experimental results (PDF)

■ AUTHOR INFORMATION

Corresponding Author

Dor Ben-Amotz − *Department of Chemistry, Purdue University, West Lafayette, Indiana 47907, United States;* orcid.org/0000-0003-4683-5401; Email: bendor@purdue.edu

https://doi.org/10.1021/acs.jpclett.3c02603
J. Phys. Chem. Lett. 2023, 14, 11376−11383

Authors

Andres S. Urbina − *Department of Chemistry, Purdue University, West Lafayette, Indiana 47907, United States;* orcid.org/0000-0001-6482-4736

Lyudmila V. Slipchenko − *Department of Chemistry, Purdue University, West Lafayette, Indiana 47907, United States;* orcid.org/0000-0002-0445-2990

Complete contact information is available at: https://pubs.acs.org/10.1021/acs.jpclett.3c02603

Notes

The authors declare no competing financial interest.

■ ACKNOWLEDGMENTS

The work was supported by grants from the National Science Foundation (CHE-1763581 for A.S.U. and D.B.-A. and CHE-2102639 for L.V.S.).

■ REFERENCES

(1) Ben-Amotz, D.; Mendes de Oliveira, D. Surfactant Aggregate Size Distributions Above and Below the Critical Micelle Concentration. *J. Chem. Phys.* **2021**, *155*, No. 224902.

(2) Overduin, S. D.; Perera, A.; Patey, G. N. Structural Behavior of Aqueous t-Butanol Solutions from Large-scale Molecular Dynamics Simulations. *J. Chem. Phys.* **2019**, *150*, No. 184504.

(3) Ben-Amotz, D. Water-Mediated Hydrophobic Interactions. *Annu. Rev. Phys. Chem.* **2016**, *67*, 617−638.

(4) Rankin, B. M.; Ben-Amotz, D.; van der Post, S. T.; Bakker, H. J. Contacts Between Alcohols in Water Are Random Rather than Hydrophobic. *J. Phys. Chem. Lett.* **2015**, *6*, 688−692.

(5) Ben-Amotz, D. Hydrophobic Ambivalence: Teetering on the Edge of Randomness. *J. Phys. Chem. Lett.* **2015**, *6*, 1696−1701.

(6) Wilcox, D. S.; Rankin, B. M.; Ben-Amotz, D. Distinguishing Aggregation from Random Mixing in Aqueous t-Butyl Alcohol Solutions. *Faraday Disc.* **2014**, *167*, 177−190.

(7) Overduin, S. D.; Patey, G. N. Comparison of Simulation and Experimental Results for a Model Aqueous tert-Butanol Solution. *J. Chem. Phys.* **2017**, *147*, No. 024503.

(8) Gupta, R.; Patey, G. N. Aggregation in Dilute Aqueous tert-Butyl Alcohol Solutions: Insights from Large-Scale Simulations. *J. Chem. Phys.* **2012**, *137*, No. 034509.

(9) Paul, S.; Patey, G. N. Why tert-Butyl Alcohol Associates in Aqueous Solution but Trimethylamine-N-oxide Does Not. *J. Phys. Chem. B* **2006**, *110*, 10514−10518.

(10) Artola, P. A.; Raihane, A.; Crauste-Thibierge, C.; Merlet, D.; Emo, M.; Alba-Simionesco, C.; Rousseau, B. Limit of Miscibility and Nanophase Separation in Associated Mixtures. *J. Phys. Chem. B* **2013**, *117*, 9718−27.

(11) Wojtków, D.; Czarnecki, M. A. Effect of Temperature and Concentration on the Structure of tert-Butyl Alcohol/Water Mixtures: Near-Infrared Spectroscopic Study. *J. Phys. Chem. A* **2005**, *109*, 8218−8224.

(12) Ben-Amotz, D.; Rankin, B. M.; Widom, B. Molecular Aggregation Equilibria. Comparison of Finite Lattice and Weighted Random Mixing Predictions. *J. Phys. Chem. B* **2014**, *118*, 7878−7885.

(13) Rankin, B. M.; Ben-Amotz, D.; Widom, B. Finite Lattice Model for Molecular Aggregation Equilibria. Boolean Statistics, Analytical Approximations, and the Macroscopic Limit. *Phys. Chem. Chem. Phys.* **2015**, *17*, 21960−21967.

(14) Rankin, B. M.; Ben-Amotz, D. Analysis of Molecular Aggregation Equilibria Using Random Mixing Statistics. *J. Phys. Chem. B* **2013**, *117*, 15667−15674.

(15) Misawa, M.; Sato, T.; Onozuka, A.; Maruyama, K.; Mori, K.; Suzuki, S.; Otomo, T. Analysis of Small-Angle Neutron Scattering Intensity: Concentration Fluctuation in Alcohol−Water Mixtures. *J. Appl. Crystallogr.* **2007**, *40*, s93−s96.

(16) Subramanian, D.; Boughter, C. T.; Klauda, J. B.; Hammouda, B.; Anisimov, M. A. Mesoscale Inhomogeneities in Aqueous Solutions of Small Amphiphilic Molecules. *Faraday Discuss.* **2014**, *167*, 217−238.

(17) Bender, T. M.; Pecora, R. A Dynamic Light-Scattering Study of the tert-Butyl Alcohol Water-System. *J. Phys. Chem.* **1986**, *90*, 1700−1706.

(18) Comez, L.; Paolantoni, M.; Lupi, L.; Sassi, P.; Corezzi, S.; Morresi, A.; Fioretto, D. Hydrophobic Hydration in Water−tert-Butyl Alcohol Solutions by Extended Depolarized Light Scattering. *J. Phys. Chem. B* **2015**, *119*, 9236−9243.

(19) Ghysels, A.; Van Speybroeck, V.; Pauwels, E.; Catak, S.; Brooks, B. R.; Van Neck, D.; Waroquier, M. Comparative Study of Various Normal Mode Analysis Techniques Based on Partial Hessians. *J. Comput. Chem.* **2010**, *31*, 994−1007.

(20) Chen, B.; Potoff, J. J.; Siepmann, J. I. Monte Carlo Calculations for Alcohols and Their Mixtures with Alkanes. Transferable Potentials for Phase Equilibria. 5. United-Atom Description of Primary, Secondary, and Tertiary Alcohols. *J. Phys. Chem. B* **2001**, *105*, 3093−3104.

(21) Ben-Amotz, D. Electric Buzz in a Glass of Pure Water. *Science* **2022**, *376*, 800−801.

(22) Pullanchery, S.; Kulik, S.; Rehl, B.; Hassanali, A.; Roke, S. Charge Transfer across C−H···O Hydrogen Bonds Stabilizes Oil Droplets in Water. *Science* **2021**, *374*, 1366−1370.

(23) Davis, J. G.; Gierszal, K. P.; Wang, P.; Ben-Amotz, D. Water Structural Transformation at Molecular Hydrophobic Interfaces. *Nature* **2012**, *491*, 582−585.

(24) Lawton, W. H.; Sylvestre, E. A. Self Modeling Curve Resolution. *Technometrics* **1971**, *13*, 617−633.

(25) Abraham, M. J.; Murtola, T.; Schulz, R.; Páll, S.; Smith, J. C.; Hess, B.; Lindahl, E. GROMACS: High Performance Molecular Simulations through Multi-Level Parallelism from Laptops to Supercomputers. *SoftwareX* **2015**, *1−2*, 19−25.

(26) Jorgensen, W. L.; Ravimohan, C. Monte-Carlo Simulation of Differences in Free-Energies of Hydration. *J. Chem. Phys.* **1985**, *83*, 3050−3054.

(27) Jorgensen, W. L.; Tirado-Rives, J. The OPLS [Optimized Potentials for Liquid Simulations] Potential Functions for Proteins, Energy Minimizations for Crystals of Cyclic Peptides and Crambin. *J. Am. Chem. Soc.* **1988**, *110*, 1657−1666.

(28) Vanommeslaeghe, K.; Hatcher, E.; Acharya, C.; Kundu, S.; Zhong, S.; Shim, J.; Darian, E.; Guvench, O.; Lopes, P.; Vorobyov, I.; Mackerell, A. D., Jr. CHARMM General Force Field: A Force Field for Drug-like Molecules Compatible with the CHARMM All-Atom Additive Biological Force Fields. *J. Comput. Chem.* **2010**, *31*, 671−90.

(29) Abascal, J. L. F.; Vega, C. A General Purpose Model for the Condensed Phases of Water: TIP4P/2005. *J. Chem. Phys.* **2005**, *123*, No. 234505.

(30) Bussi, G.; Donadio, D.; Parrinello, M. Canonical Sampling through Velocity Rescaling. *J. Chem. Phys.* **2007**, *126*, No. 014101.

(31) Parrinello, M.; Rahman, A. Polymorphic Transitions in Single Crystals: A New Molecular Dynamics Method. *J. Appl. Phys.* **1981**, *52*, 7182−7190.

(32) Mackerell, A. D., Jr.; Feig, M.; Brooks, C. L., III Extending the Treatment of Backbone Energetics in Protein Force Fields: Limitations of Gas-Phase Quantum Mechanics in Reproducing Protein Conformational Distributions in Molecular Dynamics Simulations. *J. Comput. Chem.* **2004**, *25*, 1400−1415.

(33) Darden, T.; York, D.; Pedersen, L. Particle Mesh Ewald: An N·log (N) Method for Ewald Sums in Large Systems. *J. Chem. Phys.* **1993**, *98*, 10089−10092.

(34) Essmann, U.; Perera, L.; Berkowitz, M. L.; Darden, T.; Lee, H.; Pedersen, L. G. A Smooth Particle Mesh Ewald Method. *J. Chem. Phys.* **1995**, *103*, 8577−8593.

(35) Gordon, M. S.; Freitag, M. A.; Bandyopadhyay, P.; Jensen, J. H.; Kairys, V.; Stevens, W. J. The Effective Fragment Potential Method: A QM-Based MM Approach to Modeling Environmental Effects in Chemistry. *J. Phys. Chem. A* **2001**, *105*, 293−307.

(36) Gordon, M. S.; Smith, Q. A.; Xu, P.; Slipchenko, L. V. Accurate First Principles Model Potentials for Intermolecular Interactions. *Annu. Rev. Phys. Chem.* **2013**, *64*, 553−578.
(37) Slipchenko, L. V. Solvation of the Excited States of Chromophores in Polarizable Environment: Orbital Relaxation versus Polarization. *J. Phys. Chem. A* **2010**, *114*, 8824−8830.
(38) Slipchenko, L. V.; Gurunathan, P. K. Effective Fragment Potential Method: Past, Present, and Future. In *Fragmentation: Toward Accurate Calculations on Complex Molecular Systems*; Wiley, 2017; pp 183−208. .
(39) Schmidt, M. W.; Baldridge, K. K.; Boatz, J. A.; Elbert, S. T.; Gordon, M. S.; Jensen, J. H.; Koseki, S.; Matsunaga, N.; Nguyen, K. A.; Su, S.; Windus, T. L.; Dupuis, M.; Montgomery, J. A., Jr General Atomic and Molecular Electronic Structure System. *J. Comput. Chem.* **1993**, *14*, 1347−1363.
(40) Barca, G. M. J.; Bertoni, C.; Carrington, L.; Datta, D.; De Silva, N.; Deustua, J. E.; Fedorov, D. G.; Gour, J. R.; Gunina, A. O.; Guidez, E.; Harville, T.; Irle, S.; Ivanic, J.; Kowalski, K.; Leang, S. S.; Li, H.; Li, W.; Lutz, J. J.; Magoulas, I.; Mato, J.; Mironov, V.; Nakata, H.; Pham, B. Q.; Piecuch, P.; Poole, D.; Pruitt, S. R.; Rendell, A. P.; Roskop, L. B.; Ruedenberg, K.; Sattasathuchana, T.; Schmidt, M. W.; Shen, J.; Slipchenko, L.; Sosonkina, M.; Sundriyal, V.; Tiwari, A.; Galvez Vallejo, J. L.; Westheimer, B.; Włoch, M.; Xu, P.; Zahariev, F.; Gordon, M. S. Recent Developments in the General Atomic and Molecular Electronic Structure System. *J. Chem. Phys.* **2020**, *152*, No. 154102.
(41) Frisch, M. J.; Pople, J. A.; Binkley, J. S. Self-Consistent Molecular Orbital Methods 25. Supplementary Functions for Gaussian Basis Sets. *J. Chem. Phys.* **1984**, *80*, 3265−3269.
(42) Hands, M. D.; Slipchenko, L. V. Intermolecular Interactions in Complex Liquids: Effective Fragment Potential Investigation of Water-tert-Butanol Mixtures. *J. Phys. Chem. B* **2012**, *116*, 2775−2786.
(43) Flick, J. C.; Kosenkov, D.; Hohenstein, E. G.; Sherrill, C. D.; Slipchenko, L. V. Accurate Prediction of Noncovalent Interaction Energies with the Effective Fragment Potential Method: Comparison of Energy Components to Symmetry-Adapted Perturbation Theory for the S22 Test Set. *J. Chem. Theory Comput.* **2012**, *8*, 2835−43.
(44) Viquez Rojas, C. I.; Fine, J.; Slipchenko, L. V. Exchange-Repulsion Energy in QM/EFP. *J. Chem. Phys.* **2018**, *149*, No. 094103.
(45) Slipchenko, L. V.; Gordon, M. S. Damping Functions in the Effective Fragment Potential Method. *Mol. Phys.* **2009**, *107*, 999−1016.
(46) Li, H.; Jensen, J. H. Partial Hessian Vibrational Analysis: The Localization of the Molecular Vibrational Energy and Entropy. *Theor. Chem. Acc.* **2002**, *107*, 211−219.
(47) Besley, N. A.; Bryan, J. A. Partial Hessian Vibrational Analysis of Organic Molecules Adsorbed on Si(100). *J. Phys. Chem. C* **2008**, *112*, 4308−4314.
(48) Melendez-Pagan, Y.; Ben-Amotz, D. Intermolecular Forces and Bond Length Changes in High-Pressure Fluids. Vibrational Spectroscopic Measurement and Generalized Perturbed Hard Fluid Analysis. *J. Phys. Chem. B* **2000**, *104*, 7858−7866.

https://doi.org/10.1021/acs.jpclett.3c02603
J. Phys. Chem. Lett. 2023, 14, 11376−11383